

# SVOM discovery of a strong X-ray outburst of the blazar 1ES 1959+650 and multi-wavelength follow-up with the Neil Gehrels Swift observatory

A. Foisseau<sup>1</sup>\*, A. Coleiro<sup>1</sup>, S. Komossa<sup>2,6</sup>, D. Grupe<sup>3</sup>, F. Cangemi<sup>1</sup>, P. Maggi<sup>4</sup>, D. Götz<sup>5</sup>

H.-B. Cai<sup>6</sup>, B. Cordier<sup>5</sup>, N. Dagoneau<sup>5</sup>, Z.-G. Dai<sup>7</sup>, Y.-W. Dong<sup>8</sup>, M. Fernandes Moita<sup>5</sup>, O. Godet<sup>9</sup>, A. Goldwurm<sup>1,10</sup>, H. Goto<sup>5</sup>, S. Guillot<sup>9</sup>, L. Huang<sup>6</sup>, M.-H. Huang<sup>6</sup>, N. Jiang<sup>7</sup>, C. Lachaud<sup>1</sup>, S. Le Stum<sup>1</sup>, E.-W. Liang<sup>11</sup>, X.-M. Lu<sup>6</sup>, L. Michel<sup>4</sup>, C. Plasse<sup>5</sup>, Y.L. Qiu<sup>6</sup>, J. Rodriguez<sup>5</sup>, L. Tao<sup>8</sup>, S. Schanne<sup>5</sup>, J. Wang<sup>6</sup>, X.-G. Wang<sup>11</sup>, X.-Y. Wang<sup>12</sup>, J. Wei<sup>6,13</sup>, C. Wu<sup>6</sup>, Y.-W. Yu<sup>14</sup>, J. Zhang<sup>14</sup>, L. Zhang<sup>8</sup>, S.-N. Zhang<sup>8</sup>, and S. Zheng<sup>8</sup>

<sup>1</sup> Université Paris Cité, CNRS, Astroparticule et Cosmologie, F-75013 Paris, France

<sup>2</sup> Max-Planck-Institut für Radioastronomie, Auf dem Hügel 69, 53121 Bonn, Germany

<sup>3</sup> Department of Physics, Geology, and Engineering Technology, Northern Kentucky University, 1 Nunn Drive, Highland Heights, KY 41099, USA

<sup>4</sup> Observatoire Astronomique de Strasbourg, Université de Strasbourg, CNRS, 11 rue de l'Université, F-67000 Strasbourg, France

<sup>5</sup> Université Paris-Saclay, Université Paris Cité, CEA, CNRS, AIM, 91191, Gif-sur-Yvette, France

<sup>6</sup> National Astronomical Observatories, Chinese Academy of Sciences, Beijing 100101, People's Republic of China

<sup>7</sup> Department of Astronomy, University of Science and Technology of China, Hefei 230026, People's Republic of China

<sup>8</sup> Key Laboratory of Particle Astrophysics, Institute of High Energy Physics, Chinese Academy of Sciences, Beijing 100049, China

<sup>9</sup> IRAP, CNRS, 9 avenue du Colonel Roche, BP 44346, F-31028 Toulouse Cedex 4, France

<sup>10</sup> CEA Paris-Saclay, Irfu / D'epartement d'Astrophysique, F-91191 Gif-sur-Yvette, France

<sup>11</sup> Guangxi Key Laboratory for Relativistic Astrophysics, School of Physical Science and Technology, Guangxi University, Nanning 530004, People's Republic of China

<sup>12</sup> School of Astronomy and Space Science, Nanjing University, 210023 Nanjing, Jiangsu, China

<sup>13</sup> School of Astronomy and Space Science, University of Chinese Academy of Sciences, Beijing, People's Republic of China

<sup>14</sup> School of Physics, Beijing Institute of Technology, Beijing 100081, People's Republic of China

January 23, 2026

## ABSTRACT

**Context.** On December 6, 2024, 1ES 1959+650, one of the X-ray brightest blazars known, underwent a high-amplitude X-ray outburst detected by SVOM, the first such discovery with this mission. The source was subsequently monitored with SVOM and *Swift* from December 2024 to March 2025.

**Aims.** We report the detection and multi-wavelength follow-up of this event, and describe the temporal and spectral evolution observed during the campaign.

**Methods.** Data from SVOM/MXT, SVOM/ECLAIRs, and *Swift*/XRT were analyzed with log-parabola models to track flux and spectral variability.

**Results.** The source was detected in a bright state over the 0.3–50 keV range. During the three months of monitoring, the X-ray flux varied significantly, showing episodes of spectral hardening at high flux levels. The spectral curvature evolved more irregularly and did not show a clear trend with flux. A shift of the Spectral Energy Distribution (SED) synchrotron peak to higher energies is seen when the flux increases.

**Conclusions.** This constitutes the first blazar outburst discovered in X-rays by SVOM. The coordinated follow-up with *Swift* provided continuous coverage of the flare and highlights the strong complementarity of the two missions for time-domain studies of blazars. The flare shows no clear signatures of either Fermi I or Fermi II acceleration, suggesting a mixed Fermi I/II scenario.

**Key words.** Galaxies: active – BL Lacertae objects: individual: 1ES 1959+650 – Radiation mechanisms: non-thermal – X-rays: galaxies

## 1. Introduction

Blazars are among the most extreme active galactic nuclei (AGNs), characterized by relativistic jets oriented close to the line of sight, producing strong Doppler boosting and large-amplitude variability across the electromagnetic spectrum (see, e.g., Urry & Padovani 1995). Their broad-band spectra are non-

thermal, with the low-energy component widely attributed to synchrotron emission from relativistic electrons, while the origin of the high-energy component is still debated between leptonic models and hadronic scenarios (Marscher & Gear 1985; Dermer et al. 1992; Böttcher et al. 2013). The extreme conditions in blazar jets make them bright and highly variable sources, especially at X-rays and  $\gamma$ -rays energies.

\* Corresponding author: e-mail: [foisseau@apc.in2p3.fr](mailto:foisseau@apc.in2p3.fr)

1ES 1959+650 (z = 0.0048; Krawczynski et al. 2004) is a high-synchrotron-peaked BL Lac object (HBL), with its synchrotron peak located in the Ultraviolet (UV) –X-ray range. The source was first detected in the radio and X-ray domains (Gregory & Condon 1991; Elvis et al. 1992), and later in the very-high-energy (VHE)  $\gamma$ -ray band (Nishiyama 1999) with the Whipple Observatory and the High-Energy-Gamma-Ray Astronomy (HEGRA) telescope. A major flaring episode was observed in 2002 at VHE  $\gamma$ -rays (Holder et al. 2003; Aharonian et al. 2003; Daniel et al. 2005), and since then, recurrent variability has been reported in optical (Baliyan et al. 2016), X-rays (Kapanadze et al. 2016b; Kapanadze 2018), and  $\gamma$ -rays (see, e.g., Buson et al. 2016; Biland & FACT Collaboration 2016). The source has also been studied as a potential emitter of high-energy neutrinos (Halzen & Hooper 2005) but it remains undetected.

On December 6, 2024, the Chinese–French mission SVOM (Space Variable Objects Monitor; Wei et al. 2016) detected 1ES 1959+650 in a bright X-ray flaring state (Coleiro et al. 2024), marking the first blazar outburst discovered in X-rays by SVOM. A dense follow-up campaign was carried out in coordination with the Neil Gehrels Swift Observatory (hereafter *Swift*; Gehrels et al. 2004), providing optical to X-ray coverage from December 2024 to March 2025. In this article, we report the results of this campaign and discuss the spectral and temporal properties of the flare.

Section 2 describes the detection of the outburst phase as well as the monitoring campaign with both SVOM and *Swift*. Section 3 presents the results, first describing the outburst evolution and then the spectral analysis. Section 4 is dedicated to the discussion and conclusions.

## 2. Observations and data analysis

On 2024 December 6 at 15:08:48 UT, during its commissioning phase, the SVOM/ECLAIRs telescope (4–150 keV) detected enhanced X-ray emission from the field of the BL Lac blazar 1ES 1959+650 (Coleiro et al. 2024) through the onboard trigger system. The source appeared as a previously unreported transient in ECLAIRs data, prompting rapid follow-up. A Target of Opportunity (ToO) observation was performed with SVOM, allowing MXT (0.2–10 keV) and VT (*B* and *R* filters) to acquire data starting at 16:47:41 UT, with a total exposure of 9.1 ks. During this observation, 1ES 1959+650 was detected with all three SVOM imaging instruments—ECLAIRs, MXT, and VT. The integrated 4–20 keV flux measured by ECLAIRs was approximately 2 mCrab, while MXT measured a 0.5–10 keV flux of  $\sim$ 5.5 mCrab, well above the typical unabsorbed 0.3–10 keV flux reported by Kapanadze et al. (2016b). VT observations yielded optical magnitudes of  $14.150 \pm 0.005$  and  $13.787 \pm 0.004$  in the  $VT_B$  and  $VT_R$  filters, respectively (after correction for Galactic extinction using Cardelli et al. 1989). The MXT and VT measurements confirm that the source was in a significantly high state.

To monitor the evolution of the outburst, SVOM executed nine Target-of-Opportunity (ToO) observations between December 6 and December 26, 2024. Observations ceased after December 26 due to solar constraints that rendered the source inaccessible to the satellite (Foisseau et al. 2025). *Swift* initiated follow-up observations on December 12, 2024 (Komossa et al. 2024b,a), six days after the initial SVOM detection, and continued monitoring until March 1, 2025, extending the temporal coverage of the flare. Table A.1 summarizes all observations performed with SVOM and *Swift*.

ntype Data from SVOM and *Swift* were processed using their respective official pipelines. The SVOM/ECLAIRs spectra were generated by stacking all observations obtained on the same day to improve the signal-to-noise ratio (SNR) and were binned into 15 logarithmically spaced energy bins between 4 and 150 keV. The SVOM/MXT and *Swift*/XRT spectra were rebinned to a minimum of 50 counts per bin using `ftgrouppha`, ensuring the validity of Gaussian statistics. The *Swift*/UVOT and SVOM/VT magnitudes were extracted following the standard procedures for each instrument and converted into energy fluxes. Further details on the data reduction and analysis are provided in Appendix A.

## 3. Results

### 3.1. Outburst evolution

The evolution of the 0.3–10 keV energy flux as measured by SVOM/MXT, ECLAIRs, and *Swift*/XRT, as well as the UV/optical flux measured by SVOM/VT and *Swift*/UVOT, is shown in Fig. 1.

For all days with simultaneous soft X-ray and ECLAIRs coverage, we performed joint spectral fits combining the MXT and/or XRT spectra with that of ECLAIRs. A multiplicative constant accounted for intercalibration offsets, using XRT as the reference (fixed to 1.0), while MXT and ECLAIRs constants were left free (see Table B.1). After 2024 December 26, only XRT data were available due to SVOM operational constraints (see Table A.1), and only XRT spectra were fitted.

Spectra were modeled in XSPEC version 12.14.0 using an absorbed log-parabolic model (`constant*TBabs*logpar`; Wilms et al. 2000; Massaro et al. 2004), where `TBabs` accounts for Galactic absorption and the log-parabola is defined as

$$F(E) = K \left( \frac{E}{E_1} \right)^{-(\alpha + \beta \log(E/E_1))} \text{ ph cm}^{-2} \text{ s}^{-1} \text{ keV}^{-1}. \quad (1)$$

describes the intrinsic source spectrum. The pivot energy was fixed at  $E_1 = 1$  keV and the absorption column density at the Galactic value  $N_H = 1.0 \times 10^{21} \text{ cm}^{-2}$  (Kalberla et al. 2005). The log-parabola model is described by three parameters: the photon index at 1 keV ( $\alpha$ ), the curvature parameter  $\beta$ , and the normalization  $K$ . The fitted spectral parameters for all observations are listed in Table B.1. An example of a joint fit for the 2024 December 16 observation is shown in Fig. 2.

From these parameters, we followed Massaro et al. (2004) and computed the synchrotron peak energy,  $E_p$ , and flux,  $S_p$ , as

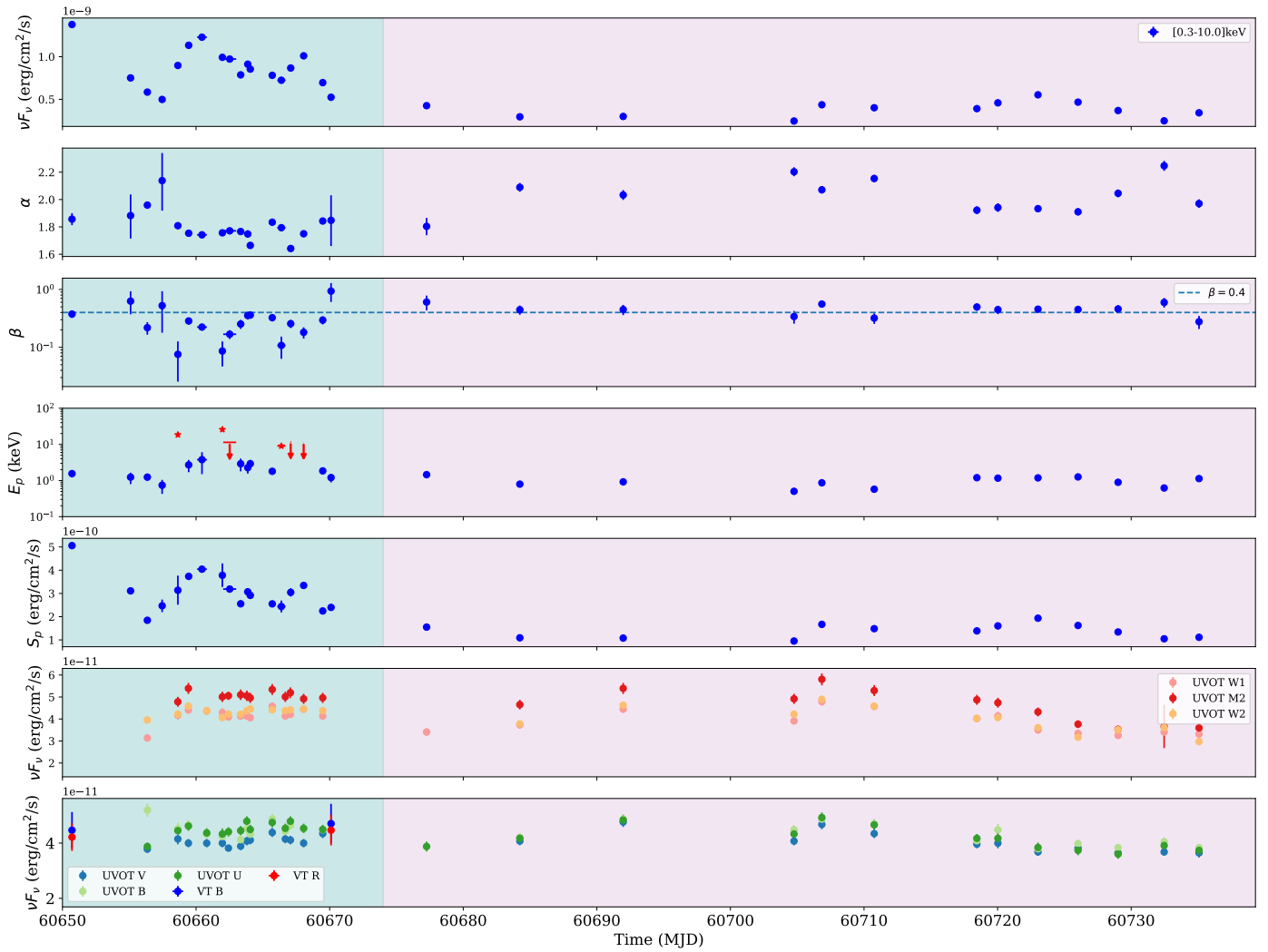
$$E_p = E_1 \cdot 10^{(2-\alpha)/(2\beta)} \text{ keV}, \quad (2)$$

$$S_p = (1.60 \times 10^{-9}) K E_1 10^{(2-\alpha)^2/(4\beta)} \text{ erg cm}^{-2} \text{ s}^{-1}. \quad (3)$$

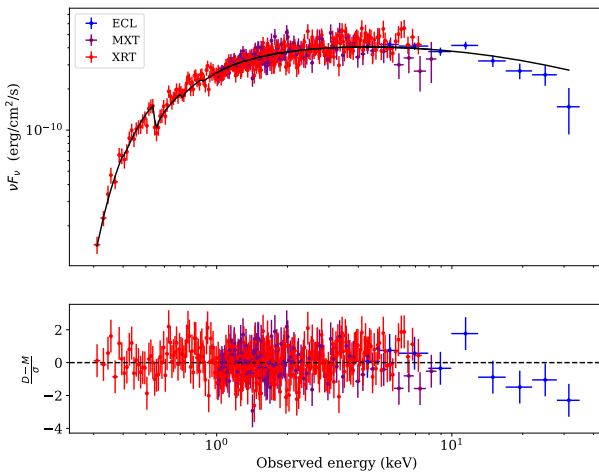
Uncertainties (68% confidence) on these two parameters were propagated from the fitted spectral parameters.

Fig. 1 shows the evolution of the X-ray and UV/optical energy flux of 1ES 1959+650 as observed throughout its outburst. The plot also shows the evolution of the fitted spectral parameters.

Two time periods can be distinguished from the 0.3–10 keV flux and  $S_p$  levels. Period 1 (2024 December 6–26) shows higher fluxes, with weighted means  $\bar{F}_{0.3-10 \text{ keV}} = (8.63 \pm 0.03) \times 10^{-10} \text{ erg cm}^{-2} \text{ s}^{-1}$  and  $\bar{S}_p = (2.50 \pm 0.01) \times 10^{-10} \text{ erg cm}^{-2} \text{ s}^{-1}$ . Period 2 (2025 January 2–March 1) shows lower values,  $\bar{F}_{0.3-10 \text{ keV}} = (3.53 \pm 0.02) \times 10^{-10} \text{ erg cm}^{-2} \text{ s}^{-1}$  and  $\bar{S}_p = (1.35 \pm 0.01) \times 10^{-10} \text{ erg cm}^{-2} \text{ s}^{-1}$ . The weighted mean photon index and curvature,  $\bar{\alpha}$  and  $\bar{\beta}$ , are given in Table 1, with weights set by the relative uncertainties of the parameters.



**Fig. 1.** Evolution of the spectral parameters and the optical to X-ray fluxes. Are presented from top to bottom : intrinsic flux in the 0.3–10.0 keV band, the photon index, the curvature parameter, the energy of the SED synchrotron peak and the associated flux, the UV (W1, M2, W2 filters) and optical (V, B, U filters, as well as the VT R and B band) fluxes. The dashed blue line in the  $\beta$  panel represent  $\beta = 0.4$ , considered as a threshold value between low and high curvature. The red stars represent points that are unconstrained whereas red triangle represent  $1\sigma$  upper limits. The blue and magenta backgrounds are respectively highlighting Period 1 and 2.



**Fig. 2.** Example of joint-fit of the XRT, MXT and ECLAIRs for the observations taken on December 16, 2024. The bottom panel shows the residuals, computed as the difference between the observed data ( $D$ ) and the model ( $M$ ), normalized by the error ( $\sigma$ ).

**Table 1.** Weighted mean values of the curvature parameter and the photon index during period 1 and 2 and during the total period.

Period	$\beta$	$\bar{\alpha}$
Period 1	$0.23 \pm 0.01$	$1.77 \pm 0.01$
Period 2	$0.44 \pm 0.02$	$2.03 \pm 0.01$
Periods 1 and 2	$0.27 \pm 0.01$	$1.85 \pm 0.01$

### 3.2. Spectral analysis

To study the correlations between the parameters, we used the Spearman rank-order correlation coefficients, which are listed in Table 2. Period 1 is characterized by harder spectra with low curvature ( $\beta < 0.4$ , the threshold distinguishing low- and high-curvature spectra) compared to Period 2 (see Table 1). The "harder when brighter" trend noted by Foisseau et al. (2025) is confirmed by the strong anti-correlation between  $\alpha$  and the 0.3–10 keV flux ( $F_{0.3-10 \text{ keV}}$ ) across the full observation campaign (Table 2). Spectra also tend to exhibit lower curvature at higher fluxes, as suggested by an anti-correlation between  $\beta$

and  $F_{0.3-10 \text{ keV}}$ . However, this trend is not statistically significant over the two periods.

A shift of the synchrotron peak energy,  $E_p$ , toward higher energies is observed with increasing flux, yielding a positive correlation between  $E_p$  and  $F_{0.3-10 \text{ keV}}$  in both periods. Such correlations are often accompanied by an anti-correlation between X-ray and radio-to-UV flux, interpreted as a long-term change in the efficiency of the particle acceleration mechanism (Katarzyński et al. 2006; Kapanadze 2018). In our observations, no anti-correlation is seen between the X-ray flux and the optical flux in the V band ( $F_V$ ), either within individual periods or in the combined dataset.

The flare shows no significant  $E_p - \beta$  anti-correlation (Table 2) in any period or in the combined dataset. Efficient stochastic acceleration is typically associated with low spectral curvature and a clear  $E_p - \beta$  anti-correlation (Tramacere et al. 2011; Massaro et al. 2011). In our case, only weak indications of this behavior are present, limited to low curvature during Period 1 and in the combined dataset (see Table 1).

To further investigate the acceleration processes, we compared the data on the  $E_p - \beta$  plane with theoretical predictions for Fermi I and Fermi II acceleration (Tramacere et al. 2011; Chen 2014), given by  $\ln(E_p) = \ln(A) + 3/(10\beta)$  and  $\ln(E_p) = \ln(A) + 3/(5\beta)$ , respectively, with  $A$  as a free parameter. Fits to Periods 1 and 2 combined yielded poor  $\chi^2$  values, preventing firm conclusions regarding the dominant acceleration process. Fits on Period 1 alone were compatible with both Fermi I and Fermi II scenarios (see Fig. 3). For Period 1, the fits resulted in  $\chi^2 = 17.9/17 = 1.05$  and  $\chi^2 = 16.8/17 = 0.99$  for the Fermi I and Fermi II scenarios, respectively, while the combined fit to Periods 1 and 2 gave  $\chi^2 = 104.1/30 = 3.47$  and  $\chi^2 = 60.9/30 = 2.03$  for Fermi I and Fermi II, respectively. We also searched for a positive  $\alpha - \beta$  correlation, expected for Fermi I (Massaro et al. 2004), but found none, either in individual periods or across the full outburst (Table 2).

A positive correlation between  $E_p$  and  $S_p$  was observed (Table 2), which is consistent with stochastic acceleration (Tramacere et al. 2011). Moreover, when the correlation follows  $S_p \propto E_p^{0.6}$ , it further indicates a transition in the turbulence energy spectrum, from a Kraichnan-type to a hard-sphere regime (Tramacere et al. 2011; Kapanadze 2018). We fitted a power-law model  $S_p = C E_p^q$  (Fig. 4), finding  $q = 3.14 \pm 2.27$ ,  $q = 1.17 \pm 0.45$ , and  $q = 1.29 \pm 0.24$  respectively for Periods 1, 2, and both combined. Large uncertainties prevent a unique physical interpretation, as the results remain compatible with multiple scenarios (Tramacere et al. 2009).

Finally, we examined the hardness ratio,  $\text{HR} = F_{2-10 \text{ keV}}/F_{0.3-2 \text{ keV}}$  (Kapanadze et al. 2018), in the  $\text{HR} - F_{0.3-10 \text{ keV}}$  plane (see Fig. 5). In stochastic acceleration, gradual electron acceleration is expected to produce counter-clockwise (CCW) loops, whereas instantaneous Fermi I acceleration may generate clockwise (CW) loops (see e.g. Cui 2004; Virtanen & Vainio 2005). A visual inspection of Fig. 5 reveals transitions between clockwise (CW) and counterclockwise (CCW) loops, a behavior commonly observed in HBLs and often interpreted as the result of shocks propagating through jet regions with varying physical conditions (Kapanadze 2018). However, an assessment of the statistical significance of these loops (see Appendix C for details) indicates that none of them are statistically significant.

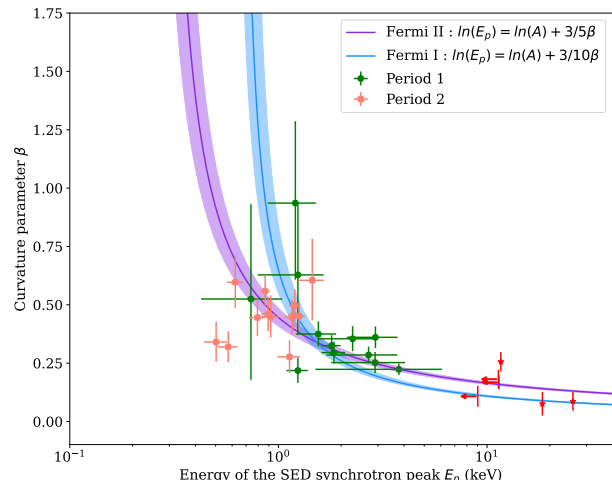


**Fig. 3.**  $E_p - \beta$  plan for the entire period (1+2). The purple and blue lines represent what we expect for Fermi II and Fermi I acceleration processes with an additional multiplicative constant fitted only using data from period 1. In both cases, the colored regions represent the error at the  $1\sigma$  level. The red stars represent points that are unconstrained whereas red triangles represent  $1\sigma$  upper limits. Errors on  $E_p$  at the  $1\sigma$  level were obtained through error propagation using the  $1\sigma$  uncertainties of the parameters  $\alpha$  and  $\beta$ . When the lower bound of the confidence interval included zero, the value was treated as a  $1\sigma$  upper limit. In addition, values were considered unconstrained when their uncertainties were at least one order of magnitude larger than the measured value itself, and when both limits of the confidence interval were poorly constrained.

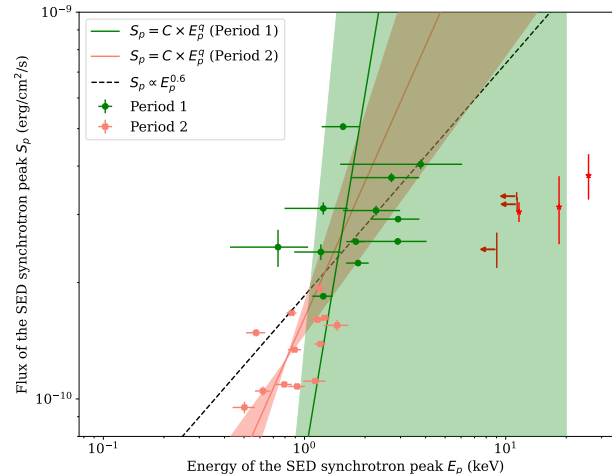


**Fig. 4.**  $S_p - E_p$  plan. The dashed line represents the case  $S_p \propto E_p^{0.6}$ . The orange and green lines represent the model  $S_p = C \times E_p^q$  fitted to the data from period 1 and period 2, respectively. In both cases, the colored region represent the error at the  $1\sigma$  level. The red stars represent points that are unconstrained whereas red triangles represent  $1\sigma$  upper limits.

## 4. Discussions and conclusions

On December 6, 2024, the ECLAIRs telescope on board SVOM detected a long X-ray transient spatially coincident with the blazar 1ES 1959+650, marking the first blazar outburst observed by SVOM (Coleiro et al. 2024). Following the trigger, SVOM performed a ToO monitoring campaign until December 26, 2024, capturing the spectral evolution of the source. *Swift* complemented these observations with 27 pointings from six days after the first detection until 2025 March 1 (Komossa et al.

**Table 2.** Spearman correlation coefficients computed for period 1 and period 2 as well as for the entire period.

Parameters	(1) $\rho$ (Period 1 + Period 2)	(2) p-value	(3) $\rho$ (Period 1)	(4) p-value	(5) $\rho$ (Period 2)	(6) p-value
$\alpha - F_{0.3-10 \text{ keV}}$	-0.83	<b><math>1.04 \times 10^{-8}</math></b>	-0.54	0.02	-0.77	<b>0.002</b>
$\beta - F_{0.3-10 \text{ keV}}$	-0.52	0.03	-0.28	0.26	0.15	0.45
$E_p - \beta$	-0.38	0.06	-0.53	0.07	0.21	0.20
$F_V - F_{0.3-10 \text{ keV}}$	0.08	0.71	-0.32	0.26	-0.01	0.97
$S_p - E_p$	0.78	<b><math>4.59 \times 10^{-6}</math></b>	0.48	0.11	0.58	0.04
$E_p - F_{0.3-10 \text{ keV}}$	0.84	<b><math>1.67 \times 10^{-7}</math></b>	0.64	0.02	0.72	0.004
$\alpha - \beta$	0.49	0.005	0.31	0.21	-0.08	0.36

**Notes.** Spearman correlation coefficients computed for period 1 and period 2 as well as for the entire period. *Column 1-2* : Spearman correlation coefficient for Periods 1 and 2 with the associated p-values. *Column 3-4* : Spearman correlation coefficient for Periods 1 with the associated p-values. *Column 5-6* : Spearman correlation coefficient for Periods 2 with the associated p-values. The correlation coefficients between  $E_p$  and another parameter do not take into account the upper limits or the unconstrained values. P-values in bold indicate correlations with a significance greater than  $3\sigma$ .

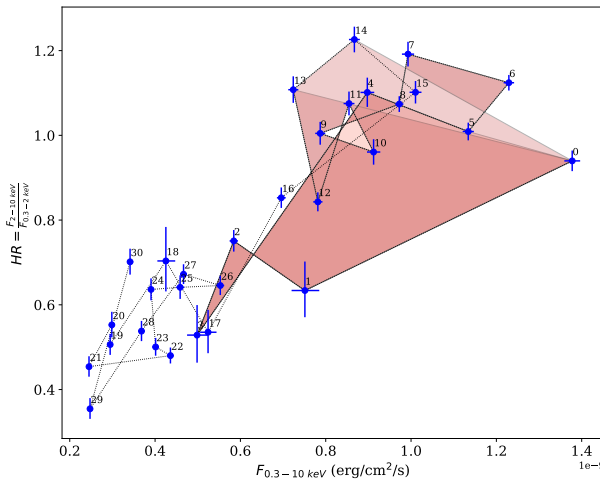


**Fig. 5.**  $HR - F_{0.3-10 \text{ keV}}$  plan for the entire follow-up campaign (period 1 and 2). The number near the data points represent the order to follow, ranging from 0 to 30. The areas shaded in orange represent the three loops initially identified and finally reject by the bootstrap algorithm. The three loops are : 0-6 CW, 0-14 CW; 0-15 CW.

2024b,a). The spectral evolution of the source was modeled using a log-parabola to identify possible correlations and tentatively probe the flare's acceleration mechanisms.

The flare exhibits a clear harder-when-brighter trend, along with a shift of the synchrotron peak energy ( $E_p$ ) toward higher energies, as indicated by the anti-correlation between  $\alpha$  and  $F_{0.3-10 \text{ keV}}$  and the positive correlation  $E_p - F_{0.3-10 \text{ keV}}$ . No corresponding decrease in the optical-to-UV flux was observed during the X-ray rise. Neither Fermi II nor Fermi I signatures were clearly detected: fitting the data to theoretical models in the  $E_p - \beta$  plane were inconclusive, and no significant  $\alpha - \beta$  correlation was observed. A positive  $S_p - E_p$  correlation was measured, consistent with stochastic acceleration, but the exponent remained poorly constrained. Similarly, no significant loops were identified in the  $HR - F_{0.3-10 \text{ keV}}$  plane, providing no clear indication of the dominant acceleration process (see Appendix C).

The absence of strong signatures from either Fermi I or Fermi II acceleration suggests that both processes may operate concurrently. Particles could undergo initial shock acceleration followed by stochastic re-acceleration downstream, or experience multiple shock crossings (Katarzyński et al. 2006; Petrosian 2012). Consequently, the combination of these mechanisms may

weaken individual signatures. Compared to previous flares of 1ES 1959+650, this event shows no clear Fermi-I or Fermi-II dominance, resembling the 2015–2016 outburst (Kapanadze et al. 2016a), whereas other flares have shown clearer stochastic acceleration signatures (see e.g. Kapanadze et al. 2018).

This study highlights the first blazar outburst detection by SVOM, demonstrating the rapid response of the satellite and collaboration with follow-up observations starting less than two hours after the trigger. The multi-day SVOM campaign, jointly with *Swift*, illustrates the SVOM mission's potential for continuous monitoring of blazar activity, providing dense temporal and spectral coverage. In particular, the low-energy threshold of ECLAIRS ensures spectral continuity beyond the 10 keV limit covered by XRT and MXT. This yields tighter constraints on physical parameters. Future SVOM observations of 1ES 1959+650, together with multi-wavelength facilities will enhance temporal and spectral sampling, offering new opportunities to probe particle acceleration mechanisms in blazar flares.

**Acknowledgements.** This work was supported by CNES, focused on SVOM. The Space-based multi-band Variable Objects Monitor (SVOM) is a joint Chinese-French mission led by the Chinese National Space Administration (CNSA), the French Space Agency (CNES), and the Chinese Academy of Sciences (CAS). We gratefully acknowledge the unwavering support of NSSC, IAM-CAS, XIOPM, NAOC, IHEP, CNES, CEA, CNRS, University of Leicester, and MPE. We would like to thank the *Swift* team for carrying out the observations we proposed. In addition to our own data, we have also used the *Swift* archive at <https://swift.gsfc.nasa.gov/archive/>. SK would like to thank the CAS President's International Fellowship Initiative for visiting scientists.

## References

- Aharonian, F., Akhperjanian, A., Beilicke, M., et al. 2003, A&A, 406, L9
- Baliyan, K. S., Chandra, S., Kaur, N., et al. 2016, The Astronomer's Telegram, 9070, 1
- Biland, A. & FACT Collaboration. 2016, The Astronomer's Telegram, 9139, 1
- Böttcher, M., Reimer, A., Sweeney, K., & Prakash, A. 2013, ApJ, 768, 54
- Braden, B. 1986, College Mathematics Journal, 17, 326
- Buson, S., Magill, J. D., Dorner, D., et al. 2016, The Astronomer's Telegram, 9010, 1
- Cardelli, J. A., Clayton, G. C., & Mathis, J. S. 1989, ApJ, 345, 245
- Chen, L. 2014, ApJ, 788, 179
- Coleiro, A., Maggi, P., Götz, D., et al. 2024, The Astronomer's Telegram, 16935, 1
- Cui, W. 2004, ApJ, 605, 662
- Daniel, M. K., Badran, H. M., Bond, I. H., et al. 2005, ApJ, 621, 181
- Dermer, C. D., Schlickeiser, R., & Mastichiadis, A. 1992, A&A, 256, L27
- Elvis, M., Plummer, D., Schachter, J., & Fabbiano, G. 1992, ApJS, 80, 257
- Fan, X., Zou, G., Wei, J., et al. 2020, in Society of Photo-Optical Instrumentation Engineers (SPIE) Conference Series, Vol. 11443, Space Telescopes and Instrumentation 2020: Optical, Infrared, and Millimeter Wave, ed. M. Lystrup & M. D. Perrin, 114430Q

Foisseau, A., Cangemi, F., Coleiro, A., et al. 2025, The Astronomer's Telegram, 16978, 1

Gehrels, N., Chincarini, G., Giommi, P., et al. 2004, ApJ, 611, 1005

Godet, O., Nasser, G., Atteia, J., et al. 2014, in Society of Photo-Optical Instrumentation Engineers (SPIE) Conference Series, Vol. 9144, Space Telescopes and Instrumentation 2014: Ultraviolet to Gamma Ray, ed. T. Takahashi, J.-W. A. den Herder, & M. Bautz, 914424

Götz, D., Boutelier, M., Burwitz, V., et al. 2023, Experimental Astronomy, 55, 487

Gregory, P. C. & Condon, J. J. 1991, ApJS, 75, 1011

Halzen, F. & Hooper, D. 2005, Astroparticle Physics, 23, 537

Holder, J., Bond, I. H., Boyle, P. J., et al. 2003, ApJ, 583, L9

Kalberla, P. M. W., Burton, W. B., Hartmann, D., et al. 2005, A&A, 440, 775

Kapanadze, B. 2018, Galaxies, 6, 125

Kapanadze, B., Dorner, D., Vercellone, S., et al. 2018, ApJS, 238, 13

Kapanadze, B., Dorner, D., Vercellone, S., et al. 2016a, MNRAS, 461, L26

Kapanadze, B., Romano, P., Vercellone, S., et al. 2016b, MNRAS, 457, 704

Katarzyński, K., Ghisellini, G., Mastichiadis, A., Tavecchio, F., & Maraschi, L. 2006, A&A, 453, 47

Komossa, S., Grupe, D., Wei, J. Y., et al. 2024a, The Astronomer's Telegram, 16955, 1

Komossa, S., Grupe, D., Wei, J. Y., & Xu, D. W. 2024b, The Astronomer's Telegram, 16941, 1

Krawczynski, H., Hughes, S. B., Horan, D., et al. 2004, ApJ, 601, 151

Marscher, A. P. & Gear, W. K. 1985, ApJ, 298, 114

Massaro, E., Perri, M., Giommi, P., & Nesci, R. 2004, A&A, 413, 489

Massaro, F., Paggi, A., & Cavaliere, A. 2011, ApJ, 742, L32

Nishiyama, T. 1999, in International Cosmic Ray Conference, Vol. 3, 26th International Cosmic Ray Conference (ICRC26), Volume 3, ed. D. Kieda, M. Salamon, & B. Dingus, 370

Petrosian, V. 2012, Space Sci. Rev., 173, 535

Tramacere, A., Giommi, P., Perri, M., Verrecchia, F., & Tosti, G. 2009, A&A, 501, 879

Tramacere, A., Massaro, E., & Taylor, A. M. 2011, ApJ, 739, 66

Urry, C. M. & Padovani, P. 1995, PASP, 107, 803

Virtanen, J. J. P. & Vainio, R. 2005, in American Institute of Physics Conference Series, Vol. 801, Astrophysical Sources of High Energy Particles and Radiation, ed. T. Bulik, B. Rudak, & G. Madejski, 410–411

Wei, J., Cordier, B., Antier, S., et al. 2016, arXiv e-prints, arXiv:1610.06892

Wilms, J., Allen, A., & McCray, R. 2000, ApJ, 542, 914

## Appendix A: Instruments and data reduction

### Appendix A.1: The SVOM space mission

SVOM has discovered 1ES 1959+650 on December 6, 2024, in an outburst phase with the ECLAIRs telescope (Coleiro et al. 2024) onboard the satellite. The outburst phase of 1ES 1959+650 has then been followed through the Target of Opportunity (ToO) program until December 26, 2024 (Foisseau et al. (2025), see Table A.1). Because of solar constraints, SVOM has not been able to observe the entire flaring phase. Note that the observations have been performed during the commissioning and verification phase of SVOM.

#### Appendix A.1.1: The ECLAIRs (4–150 keV) instrument

The ECLAIRs telescope (Godet et al. 2014, Godet et al. in prep) is a coded mask instrument with a large field of view (FoV) of  $\sim 2$  sr, operating in the 4–150 keV energy band. The data have been reduced using the official pipeline, namely ECPI version (Goldwurm et al. in prep), with the calibration files from version 20240101.

The ECPI pipeline reduces the ECLAIRs data based on the following steps. Good Time Intervals (GTIs) are defined, and energy calibration of the events is performed by applying a pixel gain and offset, while events that are not valid are flagged. Binned detector images are then created and corrected for efficiency, non-uniformity, and background. Sky images are finally reconstructed through deconvolution and coding-noise cleaning. Based on the source position in the sky images, ECPI builds a specific shadowgram model, which is fitted to the detector maps to extract the flux in each energy bin, while a second-degree polynomial accounts for the background component.

We considered all the observations in which 1ES 1959+650 was detected. For each observation considered, a spectrum was produced with 15 bins logarithmically distributed over the entire ECLAIRs energy band. The response matrix file and the ancillary response file used were respectively ECL-RSP-RMF\_20220515T01.fits and ECL-RSP-ARF\_20220515T01.fits. To increase the signal-to-noise ratio of the spectrum, we then combined the spectra from observations taken on the same day.

#### Appendix A.1.2: The MXT (0.3–10 keV) instrument

The MXT telescope (Microchannel X-ray Telescope, Götz et al. 2023, Götz et al. in prep) has a  $58 \times 58$  arcmin squared FoV, operating in the 0.3–10 keV energy band. For every observation, the data have been reduced and the spectra produced using the official pipeline, called MXT-pipeline (Maggi et al. in prep), in its 1.9.0 version. The response matrix file and ancillary response file used in the analysis were MXT-GND-MATRIX-ALL\_20250206T093900\_20240315113300.2.fits and MXT\_FM\_PANTER\_FULL-ALL-1.1.arf. The background file used was produced with the MXT-pipeline task. Because of instrumental calibration issues, we chose to consider the data only above 1.0 keV. Also, to ensure the possibility of using the Gaussian approximation, we binned the spectra with at least 50 cts/bin using ftgrouppha, developed as part of the HEASoft suite.

#### Appendix A.1.3: The VT optical telescope

The VT telescope (Visible Telescope, Fan et al. 2020, Qiu et al. in prep) is an optical telescope (40 cm aperture size) operating

with two filters: the  $VT_B$  (400–650 nm) and  $VT_R$  (650–1000 nm) bands, with a field of view (FoV) of  $26'$  in diameter. The data were analyzed following the standard procedure. 1ES 1959+650 has been observed by the VT only for two observations, taken on December 6 and December 26, 2024 (Foisseau et al. 2025).

The magnitudes were measured in the AB reference system. They were corrected for extinction following Cardelli et al. (1989). The corrected magnitudes were then converted into energy fluxes by adopting effective wavelengths of  $\lambda_R = 789.6 \pm 94.0$  nm and  $\lambda_B = 533.7 \pm 78.5$  nm for the R and B filters, respectively. Flux uncertainties were computed via error propagation, taking into account the uncertainties on the magnitudes as well as on the reference wavelengths for each filter. An error of 5% has been assumed on the magnitude values (internal communication).

#### Appendix A.2: SVOM trigger and alert system

On Friday, December 6 at 15:08:48 UT ( $T_b$ ), the on-board trigger software of the ECLAIRs telescope detected and localized a long-duration soft X-ray transient at  $RA = 300.202^\circ$ ,  $DEC = 65.182^\circ$  (J2000). The source position is constrained within a 9.3 arcmin uncertainty radius in the 5–8 keV energy band, during a 22-min exposure starting at  $T_b$ . A subsequent alert with  $SNR = 7.2$  was issued in the same band during an 11-minute exposure beginning at 15:14:15 UT. The sub-image transmitted in near real-time via the SVOM VHF network revealed a clear point-like source absent from the on-board catalog.

Following this trigger, a Target of Opportunity (ToO) observation with MXT and VT was carried out at 16:47:41 UT, with an exposure of 3.6 ks. A single source was detected at  $RA = 300.0125^\circ$ ,  $DEC = 65.1519^\circ$  (J2000), with a positional uncertainty of 25 arcsec (90% confidence level). This source lies 22 arcsec from the BL Lac blazar 1ES 1959+650.

#### Appendix A.3: The Swift Neil Gehrels Observatory

1ES 1959+650 was followed up with the Neil Gehrels Swift Observatory (Gehrels et al. 2004) in the period December 12, 2024 to March 01, 2025, starting 6 days after the initial SVOM discovery of the X-ray outburst (Komossa et al. 2024b,a, see Table A.1). In addition to our own *Swift* follow-ups, we also analyzed archival *Swift* observations from that epoch. For comparison with the ongoing outburst, we also analyzed earlier *Swift* observations from August 2024 when the blazar was found to be in its intermediate-to-low state.

#### Appendix A.3.1: The XRT (0.3–10 keV) telescope

The *Swift* X-ray telescope (XRT) observations were carried out in windowed timing (WT) mode because of the high X-ray count rate. Data were reduced with the XRTPipeline 0.13.7, that is part of the HEASoft package 6.35.1. For spectral analysis the response file swxwt0s6\_20210101v016.rmf was used. Source counts were extracted in a rectangular region of radius 40x3 pixels. Source spectra of each epoch were produced and fitted with a single powerlaw model with absorption fixed at the Galactic value of  $1.0 \times 10^{21} \text{ cm}^{-2}$  (Kalberla et al. (2005)), and free photon index  $\Gamma$ .

During the *Swift* observations, the X-ray count rate varied by a factor  $\sim 4.6$  and the peak flux was reached on December 16, 2024. A very strong anti-correlation between X-ray flux and spectral index  $\Gamma$  is immediately evident (see Fig. A.1). For fur-

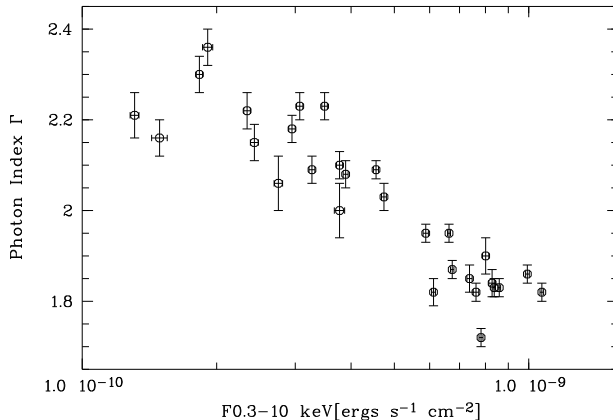


**Fig. A.1.** Power-law photon index  $\Gamma$  as function of the 0.3–10 keV flux of the XRT observations of 1ES 1959+650 between August 2024 and March 2025. The Spearman correlation coefficient  $\rho = -0.89$  determined with a p-value  $p = 5 \times 10^{-11}$ .

ther analysis, the *Swift*/XRT and SVOM X-ray data were combined. For the following analysis, to ensure the possibility to use a Gaussian approximation, we binned the spectra with at least 50 cts/bin using `ftgrouppha`.

#### Appendix A.3.2: The UVOT (UV/optical) telescope

1ES 1959+650 was also observed with the *Swift* UV-optical telescope (UVOT) in all three optical and three UV filters in order to ensure good SED coverage of this highly variable blazar. The UVOT data of each segment were co-added using the task `uvotsum`. Source counts were extracted in a circular region of radius 5 arcseconds. UVOT magnitudes were measured following standard procedures and were corrected for Galactic extinction based on Cardelli et al. (1989). The optical–UV emission was also found to be in a high state. However, it did not closely follow the X-ray evolution. The optical maximum was reached on January 31, 2025, which is 56 days after the observed X-ray peak on December 6, 2024.

#### Appendix B: Long-term spectral parameter evolution

Table B.1 provides the fitted spectral parameters for each dataset considered in our work. As explained in Section 3.1, the outburst phase can be divided into two distinct periods. The first period (2024 December 6–26), covered by both SVOM and *Swift*, shows a high flux level in the 0.3–10 keV band ( $\bar{F}_{0.3-10 \text{ keV}} = (8.63 \pm 0.03) \times 10^{-10} \text{ erg cm}^{-2} \text{ s}^{-1}$ ), with a hard spectrum combined with low curvature ( $\bar{\beta} < 0.4$ , see Table 1). In contrast, the second period (2025 January 2–March 1), covered solely by *Swift*, exhibits a lower spectral flux in the same energy band ( $\bar{F}_{0.3-10 \text{ keV}} = (3.53 \pm 0.02) \times 10^{-10} \text{ erg cm}^{-2} \text{ s}^{-1}$ ), along with a softer spectrum and higher curvature ( $\bar{\beta} > 0.4$ ). Meanwhile, the optical and UV fluxes, computed in the V and W1 bands respectively, show slightly higher values during period 2 ( $\bar{F}_V = (4.07 \pm 0.15) \times 10^{-11} \text{ erg cm}^{-2} \text{ s}^{-1}$  and  $\bar{F}_{W1} = (3.83 \pm 0.05) \times 10^{-11} \text{ erg cm}^{-2} \text{ s}^{-1}$ ) compared to period 1 ( $\bar{F}_V = (3.59 \pm 0.03) \times 10^{-11} \text{ erg cm}^{-2} \text{ s}^{-1}$  and  $\bar{F}_{W1} = (3.27 \pm 0.03) \times 10^{-11} \text{ erg cm}^{-2} \text{ s}^{-1}$ ).

#### Appendix C: Search for hysteresis in the HR – $F_{0.3-10 \text{ keV}}$ plane

To quantify the presence of loops in the HR –  $F_{0.3-10 \text{ keV}}$  plane, we computed the area enclosed by successive time-ordered observations. The area was calculated using the Gauss (shoelace) formula (Braden 1986). Each loop was required to contain at least three points. For the  $i$ -th loop, defined by observations with indices ranging from  $k_{\min}$  to  $k_{\max}$ , the enclosed area is given by

$$a_i = \frac{1}{2} \sum_{k=k_{\min}}^{k_{\max}} (F_{0.3-10 \text{ keV},k} \cdot HR_{k+1} - F_{0.3-10 \text{ keV},k+1} \cdot HR_k). \quad (\text{C.1})$$

With this convention, negative (positive) areas correspond to CW (CCW) rotations. Applying this method to all possible sequences yielded 435 candidate loops. To assess their statistical significance, we performed 10,000 bootstrap simulations by randomizing the observation indices. The resulting distributions of simulated loop areas showed that none of the observed loops exceed a significance of  $3\sigma$ .

**Table A.1.** Summary of the joint-observation campaign of SVOM and Swift for the outburst phase of 1ES 1959+650 from December 6, 2024 to March 01, 2025.

Date (1)	SVOM ObsID (2)	MXT $t_{\text{exp}}$ (s) (3)	XRT ObsID (4)	XRT $t_{\text{exp}}$ (s) (5)	ECLAIRs $t_{\text{exp}}$ (s) (6)
24/12/06	1426066399	9157.4	—	—	16635.2
24/12/11	1140853734	2084.5	—	—	6240
24/12/12	—	—	00013906125	903.1	—
24/12/13	1140853773	2083.0	—	—	1365
24/12/14	—	—	00013906126	674.1	1449
24/12/15	1140853775	2079.3	00013906129	942.0	1411.1
24/12/16	1140853776	2085.5	00013906131	838.8	5695
24/12/17	—	—	00013906132	917.3	—
24/12/18	1140853785	3786.2	00013906133	1820.8	6727.1
24/12/19 AM	—	—	00013906134	908.1	—
24/12/19 PM	1140853847	3535.1	00013906135	908.1	9848.1
24/12/20	—	—	00013906136	1022.5	—
24/12/21	—	—	00013906137	938.2	—
24/12/22	1140853853	1529.1	00013906138	918.1	3059.1
24/12/23	1140853852	1436.0	00013906139	855.6	5349.3
24/12/24	—	—	00013906140	928.1	—
24/12/25	—	—	00013906141	929.2	—
24/12/26	1140853913	3016.75	—	—	3300.1
25/01/02	—	—	00013906142	209.4	—
25/01/09	—	—	00013906144	863.2	—
25/01/16	—	—	00013906145	703.3	—
25/01/29	—	—	00013906147	1117.8	—
25/01/31	—	—	00013906148	917.8	—
25/02/04	—	—	00013906149	893.1	—
25/02/12	—	—	00013906151	908.1	—
25/02/14	—	—	00013906152	666.3	—
25/02/17	—	—	00013906153	924.3	—
25/02/20	—	—	00013906154	952.2	—
25/02/23	—	—	00013906155	883.1	—
25/02/26	—	—	00013906156	738.6	—
25/03/01	—	—	00013906157	839.4	—

**Notes.** Column (1) represent the day where the observations were performed. Column (2-3) give the SVOM ObsID and MXT exposure time (in seconds) respectively. Column (4-5) give the XRT ObsID and exposure time (in seconds). Column (6) represent the exposure of the stacked ECLAIRs spectrum of the day. Note that on December 19, 2024, two XRT observations were performed, that is why we distinguish them for this day.

**Table B.1.** Spectral parameters.

Date (1)	$\alpha$ (2)	$\beta$ (3)	$F_{0.3-10\text{ keV}}$ (4)	$E_p$ [keV] (5)	$S_p$ (6)	$C_{MXT}$ (7)	$C_{ECL}$ (8)	$\chi^2/\text{dof}$ (9)
24/12/06	$1.856^{+0.043}_{-0.044}$	$0.375^{+0.054}_{-0.052}$	$1.378^{+0.019}_{-0.018}$	$1.55^{+0.34}_{-0.34}$	$5.06^{+0.10}_{-0.10}$	—	$1.15^{+0.07}_{-0.06}$	1.20/197
24/12/11	$1.883^{+0.168}_{-0.154}$	$0.628^{+0.301}_{-0.256}$	$0.751^{+0.034}_{-0.031}$	$1.24^{+0.41}_{-0.44}$	$3.11^{+0.11}_{-0.11}$	—	$1.15^{+0.29}_{-0.23}$	0.80/72
24/12/12	$1.959^{+0.023}_{-0.023}$	$0.218^{+0.053}_{-0.054}$	$0.584^{+0.010}_{-0.010}$	$1.24^{+0.14}_{-0.15}$	$1.84^{+0.02}_{-0.02}$	—	—	1.05/163
24/12/13	$2.138^{+0.201}_{-0.220}$	$0.525^{+0.406}_{-0.346}$	$0.498^{+0.025}_{-0.023}$	$0.74^{+0.30}_{-0.31}$	$2.47^{+0.27}_{-0.27}$	—	$0.89^{+0.68}_{-0.56}$	1.13/60
24/12/14	$1.809^{+0.025}_{-0.025}$	$0.076^{+0.050}_{-0.051}$	$0.897^{+0.016}_{-0.016}$	$18.42^{\dagger}$	$3.14^{+0.63}_{-0.62}$	—	$0.96^{+0.15}_{-0.14}$	1.05/170
24/12/15	$1.754^{+0.018}_{-0.018}$	$0.285^{+0.036}_{-0.035}$	$1.134^{+0.013}_{-0.013}$	$2.70^{+1.01}_{-1.01}$	$3.73^{+0.10}_{-0.10}$	$1.25^{+0.02}_{-0.02}$	$1.08^{+0.14}_{-0.14}$	1.07/353
24/12/16	$1.742^{+0.018}_{-0.017}$	$0.223^{+0.024}_{-0.024}$	$1.229^{+0.012}_{-0.012}$	$3.78^{+2.30}_{-2.28}$	$4.04^{+0.12}_{-0.12}$	$1.90^{+0.03}_{-0.03}$	$2.00^{+0.09}_{-0.08}$	0.94/380
24/12/17	$1.757^{+0.020}_{-0.020}$	$0.086^{+0.040}_{-0.040}$	$0.993^{+0.014}_{-0.014}$	$25.81^{\dagger}$	$3.78^{+0.51}_{-0.50}$	—	—	1.07/227
24/12/18	$1.771^{+0.015}_{-0.016}$	$0.168^{+0.029}_{-0.029}$	$0.972^{+0.010}_{-0.010}$	< 11.4	$3.19^{+0.14}_{-0.14}$	$0.82^{+0.02}_{-0.01}$	$0.60^{+0.07}_{-0.07}$	1.14/398
24/12/19 AM	$1.766^{+0.022}_{-0.022}$	$0.252^{+0.045}_{-0.045}$	$0.787^{+0.012}_{-0.012}$	$2.91^{+1.14}_{-1.12}$	$2.55^{+0.03}_{-0.04}$	—	—	1.04/205
24/12/19 PM	$1.750^{+0.027}_{-0.027}$	$0.354^{+0.054}_{-0.052}$	$0.912^{+0.016}_{-0.015}$	$2.27^{+0.72}_{-0.72}$	$3.07^{+0.09}_{-0.09}$	$1.01^{+0.02}_{-0.02}$	$0.93^{+0.10}_{-0.09}$	1.13/255
24/12/20	$1.664^{+0.023}_{-0.023}$	$0.361^{+0.046}_{-0.047}$	$0.855^{+0.013}_{-0.013}$	$2.92^{+0.81}_{-0.79}$	$2.92^{+0.04}_{-0.04}$	—	—	0.88/209
24/12/21	$1.834^{+0.021}_{-0.021}$	$0.325^{+0.044}_{-0.045}$	$0.782^{+0.011}_{-0.011}$	$1.81^{+0.19}_{-0.19}$	$2.55^{+0.03}_{-0.03}$	—	—	0.98/211
24/12/22	$1.794^{+0.023}_{-0.023}$	$0.108^{+0.045}_{-0.044}$	$0.724^{+0.012}_{-0.012}$	$9.03^{\dagger}$	$2.44^{+0.21}_{-0.21}$	$1.54^{+0.04}_{-0.04}$	$1.15^{+0.13}_{-0.13}$	1.19/235
24/12/23	$1.642^{+0.022}_{-0.022}$	$0.256^{+0.042}_{-0.041}$	$0.867^{+0.013}_{-0.013}$	< 11.45	$3.05^{+0.18}_{-0.18}$	$1.06^{+0.03}_{-0.03}$	$0.84^{+0.09}_{-0.09}$	1.27/269
24/12/24	$1.750^{+0.020}_{-0.020}$	$0.181^{+0.040}_{-0.040}$	$1.010^{+0.014}_{-0.014}$	< 11.34	$3.34^{+0.08}_{-0.08}$	—	—	1.19/232
24/12/25	$1.843^{+0.022}_{-0.022}$	$0.295^{+0.047}_{-0.048}$	$0.696^{+0.010}_{-0.010}$	$1.85^{+0.24}_{-0.24}$	$2.25^{+0.03}_{-0.03}$	—	—	1.09/193
24/12/26	$1.848^{+0.183}_{-0.188}$	$0.936^{+0.328}_{-0.351}$	$0.524^{+0.020}_{-0.019}$	$1.36^{+0.31}_{-0.31}$	$2.40^{+0.11}_{-0.11}$	—	$1.20^{+0.48}_{-0.41}$	0.91/75
25/01/02	$1.804^{+0.065}_{-0.062}$	$0.605^{+0.172}_{-0.179}$	$0.425^{+0.022}_{-0.020}$	$1.45^{+0.20}_{-0.20}$	$1.55^{+0.05}_{-0.05}$	—	—	1.12/33
25/01/09	$2.089^{+0.032}_{-0.032}$	$0.445^{+0.080}_{-0.082}$	$0.295^{+0.006}_{-0.006}$	$0.79^{+0.07}_{-0.07}$	$1.09^{+0.02}_{-0.02}$	—	—	1.23/87
25/01/16	$2.033^{+0.036}_{-0.035}$	$0.449^{+0.089}_{-0.092}$	$0.299^{+0.007}_{-0.007}$	$0.92^{+0.09}_{-0.09}$	$1.08^{+0.02}_{-0.02}$	—	—	0.83/79
25/01/29	$2.183^{+0.033}_{-0.034}$	$0.387^{+0.087}_{-0.085}$	$0.245^{+0.005}_{-0.005}$	$0.58^{+0.06}_{-0.06}$	$0.93^{+0.03}_{-0.03}$	—	—	1.08/87
25/01/31	$2.071^{+0.026}_{-0.026}$	$0.559^{+0.066}_{-0.067}$	$0.436^{+0.007}_{-0.007}$	$0.86^{+0.05}_{-0.05}$	$1.67^{+0.02}_{-0.02}$	—	—	0.99/142
25/02/04	$2.154^{+0.027}_{-0.026}$	$0.320^{+0.066}_{-0.067}$	$0.401^{+0.007}_{-0.007}$	$0.57^{+0.06}_{-0.06}$	$1.48^{+0.03}_{-0.03}$	—	—	0.89/123
25/02/12	$1.922^{+0.029}_{-0.028}$	$0.497^{+0.088}_{-0.069}$	$0.391^{+0.007}_{-0.007}$	$1.20^{+0.07}_{-0.08}$	$1.39^{+0.02}_{-0.02}$	—	—	1.04/116
25/02/14	$1.941^{+0.032}_{-0.031}$	$0.447^{+0.073}_{-0.075}$	$0.459^{+0.009}_{-0.009}$	$1.16^{+0.09}_{-0.09}$	$1.60^{+0.03}_{-0.03}$	—	—	0.88/101
25/02/17	$1.933^{+0.025}_{-0.025}$	$0.456^{+0.058}_{-0.059}$	$0.553^{+0.009}_{-0.009}$	$1.18^{+0.07}_{-0.07}$	$1.93^{+0.03}_{-0.03}$	—	—	1.24/162
25/02/20	$1.910^{+0.026}_{-0.026}$	$0.451^{+0.058}_{-0.059}$	$0.467^{+0.008}_{-0.008}$	$1.26^{+0.08}_{-0.08}$	$1.62^{+0.02}_{-0.02}$	—	—	0.88/152
25/02/23	$2.045^{+0.029}_{-0.028}$	$0.459^{+0.072}_{-0.073}$	$0.368^{+0.007}_{-0.007}$	$0.89^{+0.07}_{-0.07}$	$1.34^{+0.02}_{-0.02}$	—	—	1.16/112
25/02/26	$2.247^{+0.037}_{-0.036}$	$0.597^{+0.111}_{-0.114}$	$0.248^{+0.006}_{-0.006}$	$0.62^{+0.05}_{-0.05}$	$1.05^{+0.03}_{-0.03}$	—	—	1.09/70
25/03/01	$1.971^{+0.032}_{-0.031}$	$0.277^{+0.070}_{-0.071}$	$0.341^{+0.007}_{-0.007}$	$1.13^{+0.14}_{-0.14}$	$1.11^{+0.02}_{-0.02}$	—	—	1.19/95

**Notes.** Column (1): Date of the observations. Column (2): Spectral index at 1 keV. Column (3): Curvature parameter. Column (4): 0.3-10 keV unabsorbed flux in unit of  $10^{-9}$  erg cm $^{-2}$  s $^{-1}$ . Column (5): Energy of the synchrotron peak. Column (6): Flux at the synchrotron peak in unit of  $10^{-10}$  erg cm $^{-2}$  s $^{-1}$ . Column (7): Calibration constant for SVOM/MXT. Column (8): Calibration constant for SVOM/ECLAIRs. Column (9): Reduced  $\chi^2$  with the associated degree of freedom.